Postbuckling Behavior of Selected Flat Stiffened Graphite-Epoxy Panels Loaded in Compression

James H. Starnes Jr.,* Norman F. Knight Jr.,† and Marshall Rouse‡
NASA Langley Research Center, Hampton, Virginia

Results of an experimental study of the postbuckling behavior of selected flat stiffened graphite-epoxy panels loaded in compression are presented. The postbuckling response and failure characteristics of undamaged panels and panels damaged by low-speed impact are described. Each panel had four equally spaced I-shaped stiffeners and 16- or 24-ply quasi-isotropic skins. Panels with three different stiffener spacings were tested. Some undamaged specimens supported as much as three times their initial buckling load before failing. Failure of all panels initiated in a skin-stiffener interface region. Analytical results obtained from a nonlinear general shell finite element analysis computer code correlate well with typical postbuckling test results up to failure. The analytical modeling detail necessary to predict the response of a panel accurately is described. Test results show that low-speed impact damage can reduce the postbuckling strength of a stiffened panel and the skin-stiffener interface region is more sensitive to impact damage than the skin midway between stiffeners.

Introduction

CURRENT metal aircraft design practices allow skin panels of some structural components (e.g., fuselage and stabilizer panels) to buckle at load levels below the design ultimate loading condition. These structural components are designed to have postbuckling strength. Before advanced-composite structural components can be designed with similar postbuckling responses, their strength limits and failure characteristics must be well understood. Most previous work on the postbuckling behavior of compression-loaded composite structures (e.g., Refs. 1-4) has focused on analytical solutions to classical unstiffened orthotropic plate problems. Postbuckling test results for unstiffened graphite-epoxy plates loaded in compression are compared with analytical predictions in Ref. 5. The failure characteristics of these unstiffened postbuckled specimens and the effects of low-speed impact damage on their postbuckling strength are also described in Ref. 5. Only a limited amount of data has been published that describes the postbuckling behavior of stiffened graphite-epoxy panels loaded in compression (e.g., Refs. 6-8) or the effects of low-speed impact damage on their postbuckling strength.[6]

This paper presents the results of an experimental study of the postbuckling behavior of selected flat stiffened graphite-epoxy panels loaded in compression. The postbuckling response and failure characteristics of panels with 16- or 24-ply quasi-isotropic skins and with four equally spaced *I* stiffeners are described. A relatively heavy stiffener design was selected for the panels so that the nonlinear response of the panels would be primarily due to the buckling of the skins. Analytical results obtained from the STAGS nonlinear general shell analysis computer code[9] are presented for comparison with typical test results. The analytical modeling detail necessary to predict the response of a panel accurately is described also. Also presented are the results of an exploratory experimental study of the effects of low-speed impact damage on the postbuckling behavior of the panels.

Presented as Paper 82-0777 at the AIAA/ASME/ASCE/AHS 23rd Structures, Structural Dynamics and Materials Conference, New Orleans, LA, May 10-12, 1982; received July 1982; revision received Sept. 4, 1984. This paper is declared a work of the U.S. Government and therefore is in the public domain.

*Head, Structural Mechanics Branch, Structures and Dynamics Division. Member AIAA.

†Aerospace Engineer, Structural Mechanics Branch, Structures and Dynamics Division.

‡Aerospace Engineer, Structural Mechanics Branch, Structures and Dynamics Division. Member AIAA.

Test Specimens

The specimens tested in this investigation were designed and manufactured by the Lockheed-Georgia Company under NASA Contract NAS1-15949. The specimens were fabricated from commercially available unidirectional Thornel 300§ graphite fiber tapes preimpregnated with 450 K cure Narmco 5208§ thermosetting epoxy resin. Typical lamina elastic properties for this graphite-epoxy system are given in Table 1. Each specimen had four equally spaced stiffeners of the same design. Skin thickness and stiffener spacing were varied to determine the effect of skin postbuckling response on panel performance. Specimens had either 16- or 24-ply quasi-isotropic skins and either 10.2-, 14.0-, or 17.8-cm stiffener spacing. The panel lengths were selected so the initial buckling modes would have at least four longitudinal half-waves.

The panel geometry and stifffener details are shown in Fig. 1, and a typical specimen is shown in Fig. 2. Panel length L, panel width W, and stiffener spacing b are shown schematically in Fig. 1a; stiffener geometry is shown in Fig. 1b; and the details of the tapered stiffener attachment flange are shown in Fig. 1c. Stacking sequences for the skins, stiffener webs, and stiffener caps are given in Table 2. All specimens with 24-ply skins were fabricated to have the laminates corresponding to design 1 in Table 2. All but two specimens with 16-ply skins were fabricated to have the laminates corresponding to design 2 in Table 2 which has 50-ply stiffener caps. Two specimens with 16-ply skins and 17.8-cm stiffener spacing were fabricated with 38- and 30-ply stiffener caps to determine the effects of slightly lighter stiffeners on panel behavior. These two specimens have the laminates corresponding to designs 3 and 4 in Table 2, respectively. The panel length, panel width, and stiffener spacing dimensions of all specimens are given in Tables 3 and 4.

All specimens were cured in an autoclave using the resin manufacturer's recommended procedure. The stiffeners of all of the specimens with 24-ply skins were cocured with the skins. The stiffeners of all of the specimens with 16-ply skins were secondarily bonded to the skins with 395 K cure American Cyanamid FM-73§ adhesive. Following cure, the specimens were ultrasonically inspected to establish the specimen quality. Specimens with 24-ply skins had some

§Identification of commercial products and companies in this paper is used to describe the test materials adequately. The identification of these commercial products does not constitute endorsement, expressed or implied, of such products by the National Aeronautics and Space Administration or this journal.

Table 1 Graphite-epoxy lamina properties

Longitudinal Young's modulus, GPa	131.0
Transverse Young's modulus, GPa	13.0
Shear modulus, GPa	6.4
Major Poisson's ratio	0.38
Nominal lamina thickness, mm	0.14

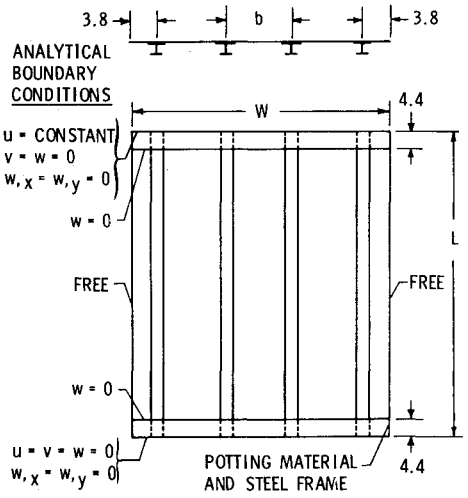

a) Panel geometry and analytical boundary conditions.

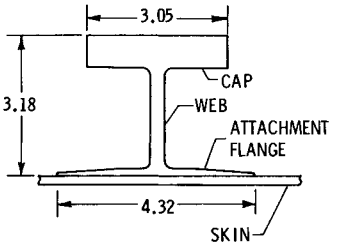

b) Stiffener geometry.

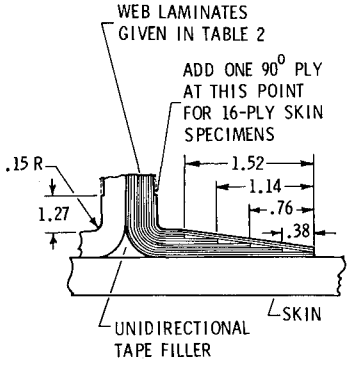

c) Stiffener attachment flange details.

Fig. 1 Panel geometry, stiffener details, and analytical boundary conditions. (All dimensions in centimeters.)

small delamination-type defects of up to 4 mm in diameter in the skins directly under the stiffeners. Specimens with 16-ply skins had no detectable defects. The ends of each specimen were potted in an epoxy resin material to prevent brooming of the graphite fibers during testing and the potting material was encased in 4.4-cm-long steel frames for protection. The loaded ends of the specimens were machined flat and parallel to permit uniform compressive loading. The unstiffened side of each specimen was painted white to reflect light so that a moire-fringe technique could be used to monitor out-of-plane deflections during testing.

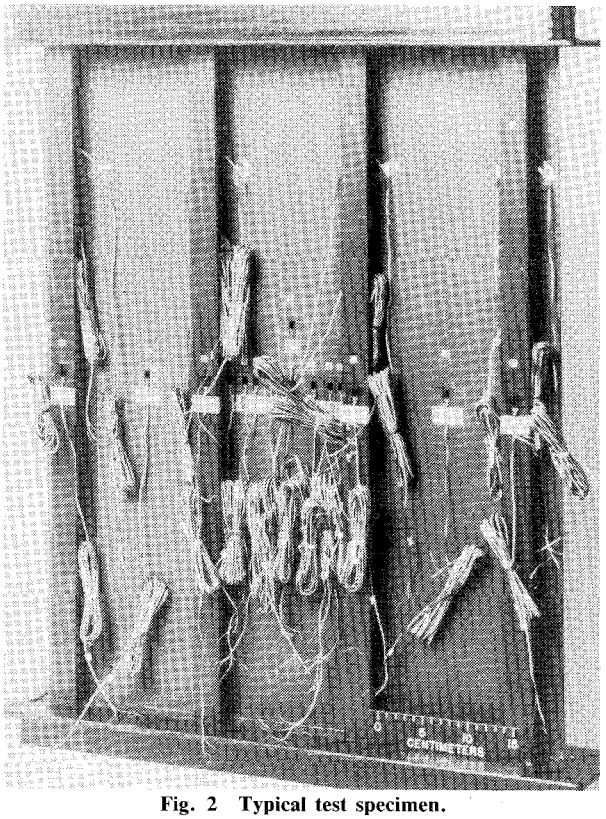

Fig. 2 Typical test specimen.

Apparatus and Tests

Test specimens were loaded in compression using a 4.45-MN-capacity hydraulic testing machine. The specimens were flat-end tested without lateral edge supports. Electrical resistance strain gages were used to monitor strains, and direct-current differential transformers were used to monitor longitudinal in-plane and out-of-plane displacements at selected locations. All electrical signals and the corresponding applied loads were recorded on magnetic tape at regular time intervals during the tests. Out-of-plane deflections were also monitored by the moire-fringe technique. Moire-fringe patterns were recorded photographically.

Eight undamaged and eight impact-damaged specimens were tested to failure in static compression to determine their postbuckling behavior. Impact damage was caused by 1.27-cm-diam aluminum spheres propelled by the air gun described in Ref. 10. Each of the impact-damaged 24-ply skin specimens was impacted once in the skin midway between two stiffeners and once in the skin at a stiffener attachment flange. Each of the impact-damaged 16-ply skin specimens was impacted only once in the skin at a stiffener attachment flange. The projectiles were directed normal to the plane of the skin at speeds ranging from 60 to 103 m/s. All specimens were impacted without any applied compressive load and then loaded to failure to determine the effect of low-speed impact damage on postbuckling behavior.

Analysis

The analyses performed in this study include both buckling and nonlinear postbuckling calculations. Buckling calculations were performed to predict the initial buckling response of the specimens and to determine the level of analytical modeling detail required to predict the postbuckling response of the specimens accurately. To determine this required level of analytical modeling detail, buckling solutions were determined using the efficient buckling analysis capability of the PASCO computer code.[11] The buckling analysis used in PASCO is based on an orthotropic

Table 2 Skin and stiffener laminates

Design	Skin	Stiffener web	Stiffener cap
1	$(\pm 45/0_2/\mp 45/90_2/\pm 45/0/90)_S$	$(90/0/\pm 45/\mp 45/0_2/\pm 45/0/90)_S$	$(90/0/\pm 45/\mp 45/0_2/\pm 45/0/90/0_3/\pm 45/0_6/\mp 45/0_3)_S$
2	$(\pm 45/0_2/\mp 45/90_2)_S$	$(0/\pm 45/\mp 45/0_2/\pm 45/0_2)_S$	$(0/\pm 45/\mp 45/0_2/\pm 45/0_2/90/0_3/90_2/0_4/90_2/0_2)_S$
3	$(\pm 45/0_2/\mp 45/90_2)_S$	$(0/\pm 45/\mp 45/0_2/\pm 45/0_2)_S$	$(0/\pm 45/\mp 45/0_2/\pm 45/0_3/90/0_3/90/0_2)_S$
4	$(\pm 45/0_2/\mp 45/90_2)_S$	$(0/\pm 45/\mp 45/0_2/\pm 45/0_2)_S$	$(0/\pm 45/\mp 45/0_2/\pm 45/0_3/90/0_2)_S$

Table 3 Results for undamaged specimens

Specimen	Width, cm	Length, cm	Stiffener spacing, cm	Analytical results: Buckling load, kN	Analytical results: End shortening at buckling, cm	Experimental results: Buckling load, kN	Experimental results: Failure load, kN	Experimental results: End shortening at failure, cm
				24-ply skins				
U1	38.1	50.8	10.2	1091	0.32	907	938	0.31
U2	49.5	66.0	14.0	596	0.21	503	719	0.28
U3	61.0	81.3	17.8	390	0.15	374	657	0.32
				16-ply skins				
U4[a]	38.1	50.8	10.2	451	0.16	356	616	0.25
U5[a]	49.5	66.0	14.0	243	0.11	205	518	0.25
U6[a]	61.0	81.3	17.8	156	0.08	138	461	0.26
U7[b]	61.0	81.3	17.8	137	0.08	125	365	0.22
U8[c]	61.0	81.3	17.8	125	0.08	120	294	0.20

[a]50-ply stiffener cap. [b]38-ply stiffener cap. [c]30-ply stiffener cap.

Table 4 Results for impact-damaged specimens

Specimen	Width, cm	Length, cm	Stiffener spacing, cm	Projectile speed, m/s	Failure load, kN	End shortening at failure, cm
				24-ply skins		
D1	38.1	50.8	10.2	68[a] 66[b]	549	0.18
D2	38.1	50.8	10.2	103[a] 100[b]	497	0.17
D3	49.5	66.0	14.0	61[a] 60[b]	492	0.17
D4	49.5	66.0	14.0	95[a] 94[b]	506	0.18
D5	61.0	81.3	17.8	69[a] 68[b]	530	0.24
D6	61.0	81.3	17.8	94[a] 95[b]	526	0.23
				16-ply skins		
D7	38.1	50.8	10.2	68[c]	377	0.14
D8	61.0	81.3	17.8	66[c]	429	0.25

[a]Impact site on skin at stiffener attachment flange I I I I.
↑

[b]Impact site on skin midway between two stiffeners I I I I.
↑

[c]Impact site on skin at stiffener attachment flange I I I I.
↑

prismatic-plate formulation and is considered to be very accurate. Since PASCO does not have a nonlinear analysis capability, the STAGS nonlinear general shell finite element analysis computer code[9] was used to perform the postbuckling analyses.

A typical buckled cross-section solution obtained from PASCO is shown in Fig. 3a for a panel with a 16-ply skin and 17.8-cm stiffener spacing. This PASCO buckling solution indicates that the stiffener webs deform and local bending occurs in the skin near the skin-stiffener interface region in much the same manner as described in Ref. 12. This buckling mode shape is characteristic of a stiffened-panel buckling mode shape as opposed to a general instability or Euler buckling mode shape. The buckling load corresponding to the stiffened-panel buckling mode shape predicted by PASCO is 151 kN, which is lower than the Euler buckling load of 393 kN. The PASCO model of the skin-stiffener region and three STAGS models with simple-support boundary conditions along the loaded edges and varying levels of modeling complexity in the skin-stiffener region are shown in Fig. 3b along with the buckled cross sections corresponding to each model. The unshaded regions of each model were represented by plates in the analyses and the shaded regions were represented by discrete beams. Buckling loads for the three STAGS models are also compared with the PASCO buckling load in Fig. 3b. The STAGS-1 model represents the stiffener entirely as a discrete beam and, as such, concentrates the extensional, bending, and torsional stiffness prop-

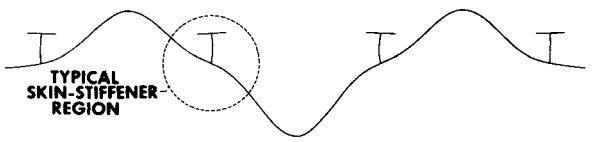

a) Buckled cross section.

ANALYTICAL MODEL	MODEL OF TYPICAL SKIN-STIFFENER REGION	BUCKLED CROSS SECTION OF TYPICAL SKIN-STIFFENER REGION	DEVIATION FROM PASCO BUCKLING RESULTS
PASCO			---
STAGS -1			-10.6%
STAGS -2			17.9%
STAGS -3			1.4%

□ ---PLATE ELEMENT ■ ---BEAM ELEMENT

b) Analytical models of the skin-stiffener region.

Fig. 3 Effect of analytical modeling detail on the buckling calculations for a specimen with a 16-ply skin and 17.8-cm stiffener spacing.

a) Stepped flange model.

b) Equivalent uniform-thickness flange model ($\bar{b}=18$ mm and $\bar{h}=1.54$ mm).

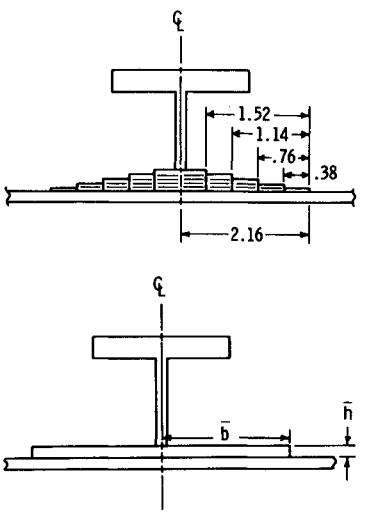

Fig. 4 Tapered attachment flange models. (Dimensions in centimeters.)

erties and the effects of stiffener eccentricities at the stiffener attachment point in the skin. This STAGS model neglects all stiffener cross-sectional deformations and prevents the local bending of the skin near the stiffener from being represented properly. By concentrating the stiffener attachment flange properties at a discrete point and not allowing the proper local skin bending to develop, the model has a larger effective stiffener spacing than actually exists and, as a consequence, the buckling load for the STAGS-1 model is 10.6% below the PASCO solution.

The STAGS-2 model represents the stiffener attachment flange as a plate and the rest of the stiffener cross section as a discrete beam. The buckling solution for the STAGS-2 model indicates that local skin deformation near the stiffener is consistent with the PASCO solution, but the stiffener cross section cannot deform. The additional stiffness provided by the rigid stiffener causes the buckling load for the STAGS-2 model to be 17.9% higher than the PASCO solution. The STAGS-3 model represents the stiffener attachment flange and the stiffener web as plates and the stiffener cap as a discrete beam. This model allows both the local bending of the skin and the cross-sectional deformation of the web to be predicted accurately. The buckling solution for this model is only 1.4% higher than the PASCO solution.

Since the stiffener attachment flange was shown to affect the panel buckling load and corresponding mode shape by influencing its effective stiffener spacing, it was assumed that an accurate model of the tapered attachment flange (see Fig. 1c) would be required for the STAGS postbuckling analysis. The STAGS postbuckling model was constructed to simulate the tapered flange and, in addition, to avoid unnecessarily high computational costs. To simulate the tapered flange, the stepped-flange model shown in Fig. 4a was developed with the appropriate stiffnesses for a PASCO analysis. Using PASCO, the buckling loads for this model were then calculated and used as a standard for comparison. Finally, the equivalent uniform-thickness flange finite element model shown in Fig. 4b was developed for STAGS by adjusting the width $\bar{b}$ and height $\bar{h}$ of the model so that the STAGS model would have the same extensional stiffness and buckling solution as the PASCO stepped-flange model.

The STAGS-3 model shown in Fig. 3b with the equivalent uniform-thickness stiffener attachment flange model shown in Fig. 4b was used to predict the postbuckling response of the specimens. The finite elements used in the STAGS model are combined membrane and bending quadrilateral elements with midside nodes. The finite element model has six plate elements across the skin between stiffeners and seven plate elements per longitudinal half-wave of the buckling mode. The stiffener web was modeled by two plate elements between the skin and the stiffener cap, and the same number of plate elements along the length as the skin. The stiffener cap was modeled as a discrete beam. The loading and boundary conditions used for the analysis were selected to be consistent with the test conditions. The loading condition corresponds to a uniform end shortening applied to one end of the specimen. The boundary conditions used for the nonlinear analyses are indicated in Fig. 1a. A linear combination of the mode shapes of the lowest two buckling loads was used to represent the initial geometric imperfections assumed to exist for the postbuckling analysis since the initial surface imperfections were not measured. The amplitudes of the buckling modes used to generate the initial geometric imperfections were assumed to be 1.0% of the skin thickness for the first mode and 0.1% for the second mode.

Results and Discussions

Undamaged Specimens

Each undamaged specimen tested in this investigation buckled into a stiffened-panel buckling mode in which both the stiffeners and the skin deformed at an applied load less than the analytically predicted buckling load. Each specimen failed at an applied load greater than the experimentally determined buckling load. The length, width, stiffener spacing, analytically predicted buckling load and corresponding end shortening, and experimentally determined buckling load, failure load, and corresponding end shortening are given in Table 3 for each undamaged specimen. Initial buckling was identified by monitoring data from back-to-back strain gages on the skin and from direct-current differential transformers that measured out-of-plane deflections of the skins. Moire-fringe patterns representing out-of-plane deflections were used to identify the buckling mode of each specimen and to visually monitor the out-of-plane deflection patterns associated with the postbuckling response of the panel skins. The buckling mode of each specimen had one transverse half-wave between each stiffener and either four (specimens U1 and U4 in Table 3) or five (all other specimens in Table 3) longitudinal half-waves. Typical moire-fringe patterns of the out-of-plane deflections for specimen U1 with an applied load equal to 938 kN just before failure and for specimen U6 with an applied load equal to 461 kN just before failure are shown in Fig. 5.

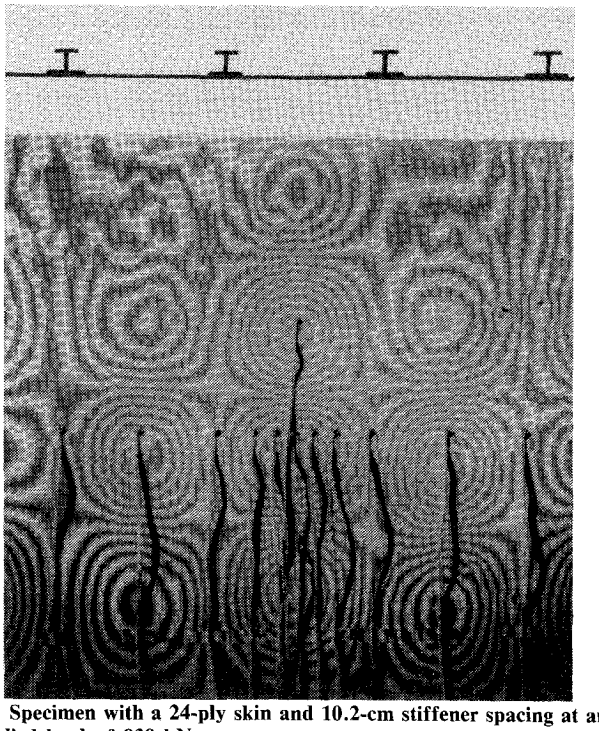

a) Specimen with a 24-ply skin and 10.2-cm stiffener spacing at an applied load of 938 kN.

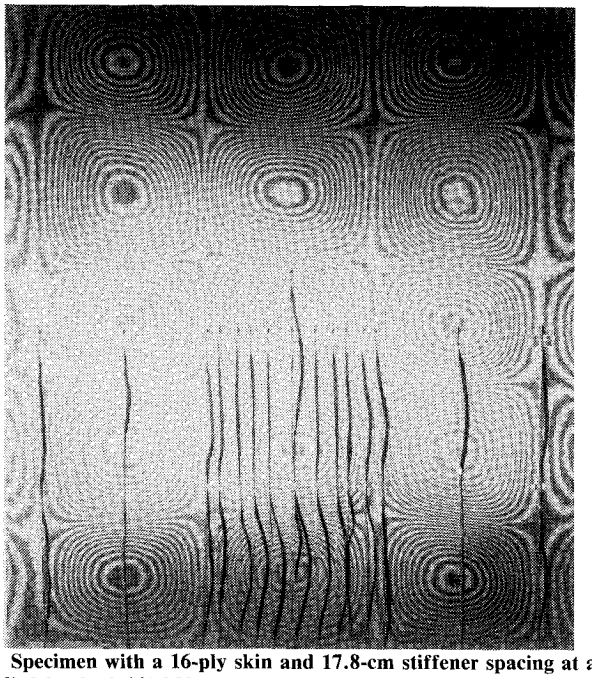

b) Specimen with a 16-ply skin and 17.8-cm stiffener spacing at an applied load of 461 kN.

Fig. 5 Moire-fringe patterns of skin buckling modes just before failure.

End-shortening results for each undamaged specimen are shown in Fig. 6 as a function of the applied compressive load. The end shortening u of each specimen is normalized by the specimen's analytical end shortening u_{cr} at buckling given in Table 3, and the applied load P is normalized by the specimen's analytical buckling load P_{cr}. The analytical buckling solution is represented in Fig. 6 by the open circle. These results indicate that the load-shortening response curves are similar for all undamaged specimens. Since all specimens buckled at applied loads less than their analytically predicted buckling loads (see Table 3), it is suspected that the specimens had varying amounts of initial geometric

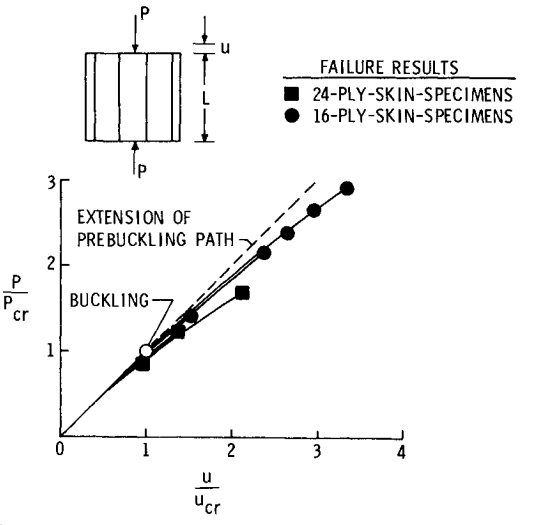

Fig. 6 End-shortening results for undamaged specimens.

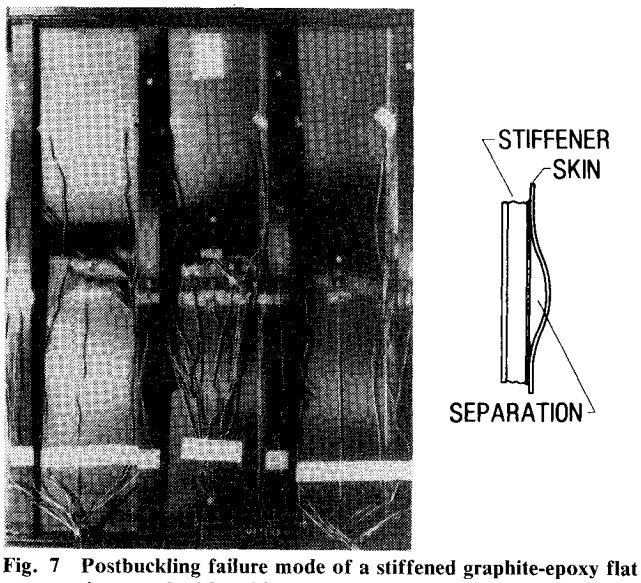

Fig. 7 Postbuckling failure mode of a stiffened graphite-epoxy flat compression panel with a 16-ply skin and 17.8-cm stiffener spacing.

imperfections that caused buckling below the predicted values. The defects found in the 24-ply skin specimens during ultrasonic inspection apparently had little effect on the buckling response of the specimens. The reduction in extensional stiffness that occurs after buckling is illustrated by the change in slope of these load-shortening response curves. The failure of each specimen is indicated in Fig. 6 by the filled symbols on the appropriate curve. The filled circles and filled squares in Fig. 6 represent the failure of the specimens with 16- and 24-ply skins, respectively. Each specimen, except specimen U1, failed at an applied load greater than its analytically predicted buckling load. Specimen U1 buckled (see Fig. 5a for the moire-fringe pattern of the skin buckling mode just before failure) and subsequently failed below the predicted buckling load.

The failure mode of all undamaged specimens was the same, and a typical failed specimen (U6) is shown in Fig. 7. Failure occurred when the skin and stiffeners separated from one another in the interior of the specimen. After the skin separated from the stiffeners, it buckled across the panel, as shown in Fig. 7. In all cases, the skin deformation mode of the failed specimen corresponds to one of the longitudinal half-wave patterns in the prefailure buckling mode.

The effect of varying stiffener spacing, skin thickness, and stiffener cap area on the postbuckling response of the un-

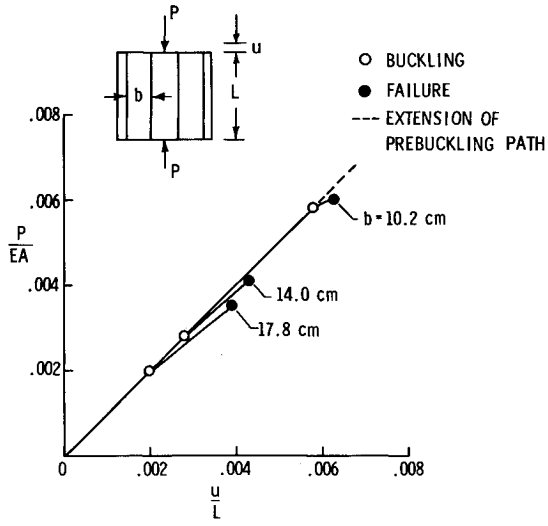

a) 24-ply skin specimens.

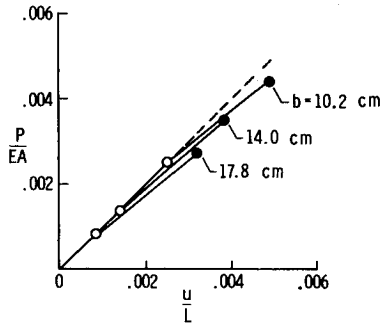

b) 16-ply skin specimens with 50-ply stiffener caps.

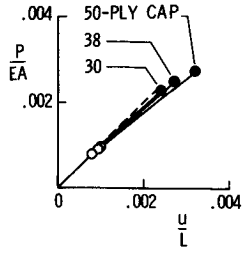

c) 16-ply skin specimens with 17.8-cm stiffener spacing and with different stiffener-cap-laminate thicknesses.

Fig. 8 End-shortening results for undamaged specimens.

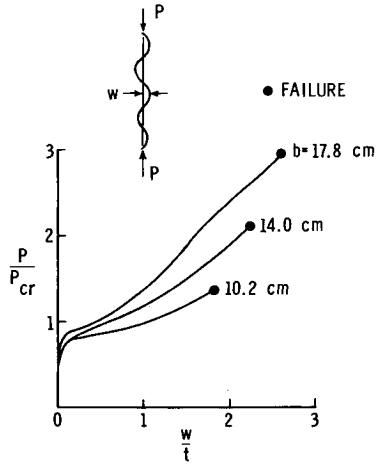

Fig. 9 Out-of-plane deflections near points of maximum buckling-mode amplitude for specimens with 16-ply skins.

damaged specimens is shown in Fig. 8. The measured end shortening u normalized by the specimen length L is shown in the figure as a function of the applied load P normalized by the specimen prebuckling extensional stiffness EA. Experimentally determined buckling results are indicated by the open circles on the figures and panel failure is indicated by the filled circles. The results indicate that each specimen has some postbuckling strength and that specimens with lower initial buckling strains can be loaded to a greater multiple of the buckling strain before failing in the postbuckling range than specimens with higher initial buckling strains. The results in Fig. 8 indicate that increasing stiffener spacing, decreasing skin thickness, or decreasing stiffener cap thickness decrease both the initial buckling strains as expected from classical buckling theory and the failure strains.

The out-of-plane deflection w measured near a point of maximum buckling-mode amplitude is shown in Fig. 9 as a function of the applied load P for three specimens with 16-ply skins (specimens U4, U5, and U6) with different stiffener spacing b. The deflection w is normalized by the specimen skin thickness t and the applied load P is normalized by the analytical buckling load P_{cr}. Failure of each specimen is indicated by a filled circle on the figure. These results indicate that large out-of-plane deflections (more than twice the skin thickness) can occur before failure.

Surface strain measurements from back-to-back strain gages at four locations on a typical specimen (i.e., U6) are shown in Fig. 10 as a function of applied load. The measured strain e is normalized by the analytical strain at buckling e_{cr} and the applied load P is normalized by the analytical buckling load P_{cr}. Data from longitudinal strain gages located at panel midlength on the skin midway between the two inner stiffeners are shown in Fig. 10a. This pair of strain gages is located near a point of maximum out-of-plane deflection of the skin buckling mode and indicates that considerable bending can occur in the skin. Data from longitudinal strain gages located at panel midlength at the stiffener attachment flange of one of the inner stiffeners are shown in Fig. 10b. One of these gages is located on the stiffener attachment flange and the other is located on the panel skin. These gages indicate that relatively large strains can occur in the stiffener attachment flange. Data from two pairs of back-to-back strain gages on the stiffener web near a quarter-point of the panel length are shown in Fig. 10c. One pair of these gages (gages A and B in Fig. 10c) is oriented in the direction of the applied load and indicates that large membrane strains exist in the stiffener web in the loading direction. The other pair of these gages (gages C and D in Fig. 10c) is oriented normal to the panel skin (transverse to the direction of the applied load) and indicates that bending of the web about the loading axis occurs after initial buckling.

The longitudinal membrane strain distribution across the center skin bay at midlength of a typical specimen (i.e., U6) is shown in Fig. 11 for three values of applied load P normalized by the analytical buckling load P_{cr}. The filled circles on the figure are the average strain e from back-to-back strain gage pairs located a distance y from the left interior stiffener. Membrane strains e are normalized by the analytical strain e_{cr} at buckling and the gage location y is normalized by the stiffener spacing b. The membrane strain distribution is uniform for loads up to the buckling load. After buckling, the strain distribution has reduced membrane strains in the center of the skin bay and increased strains near the stiffeners at the edges of the skin bay. The differences in the magnitudes of the membrane strain in the center of the skin and the membrane strain at the stiffeners become larger as the applied load is increased after buckling. The membrane strain distribution for the applied load P equal to 2.96 times the buckling load is the strain distribution just before failure and the maximum membrane strains occur at the stiffener attachment flanges. Apparently, these

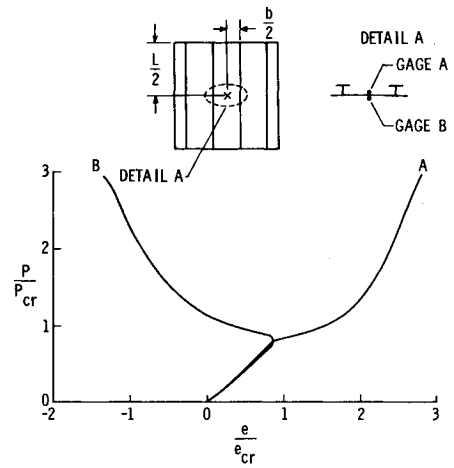

a) Skin surface strains midway between stiffeners.

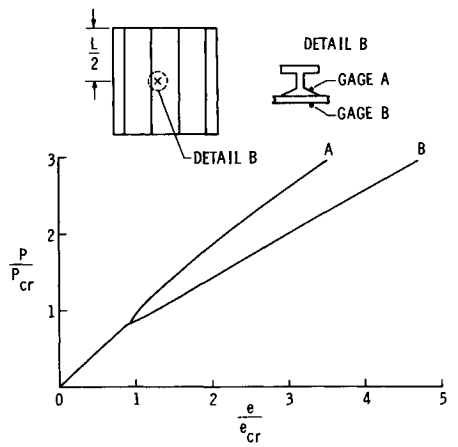

b) Surface strains on stiffener attachment flange.

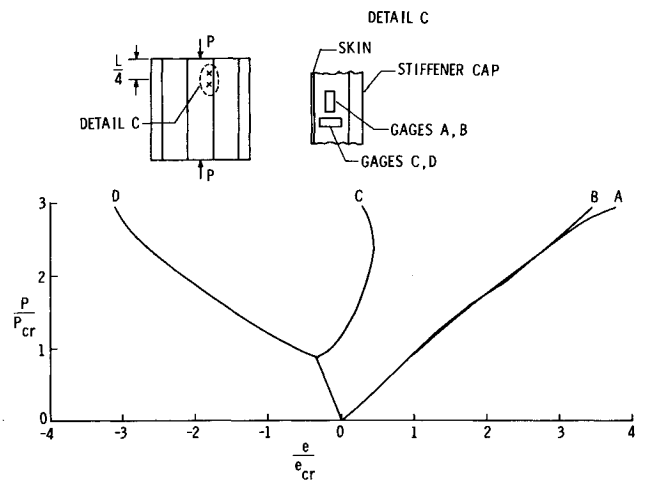

c) Strains on stiffener web.

Fig. 10 Typical strain-gage data for a specimen with 16-ply skin, 17.8-cm stiffener spacing, and 50-ply stiffener cap.

higher strains at the stiffener attachment flanges contribute to a local failure in this skin-stiffener interface region that causes panel failure. Similar membrane strain distributions for other specimens just before failure are shown in Fig. 12a for three panels with 24-ply skins (i.e., U1, U2, and U3), in Fig. 12b for three panels with 16-ply skins (i.e., U4, U5, and U6), and in Fig. 12c for three panels with 16-ply skins and different stiffener-cap-laminate thicknesses (i.e., U6, U7, and U8). The results in Figs. 12a and 12b indicate that in-

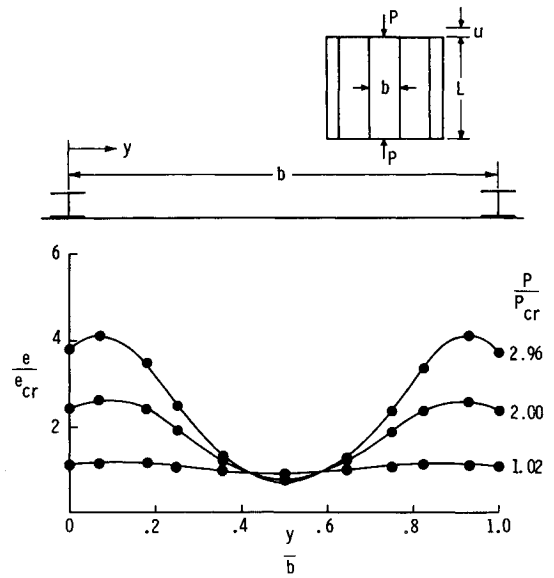

Fig. 11 Longitudinal membrane strain distribution in skin of a specimen with a 16-ply skin and 17.8-cm stiffener spacing.

creasing the stiffener spacing b of the panels decreases the membrane strain distribution across the panel. The results in Fig. 12c indicate that decreasing the stiffener-cap-laminate thickness decreases the membrane strains near the stiffeners, but has little effect on the membrane strains in the skin away from the stiffeners.

Comparisons between test and analytical results obtained with the STAGS computer code[9] are shown in Fig. 13 for a typical specimen (i.e., U6). End shortening u normalized by the analytical end shortening u_{cr} at buckling (Fig. 13a), out-of-plane deflection w near a point of maximum deflection normalized by the specimen skin thickness t (Fig. 13b), and the longitudinal surface strains e near a point of maximum out-of-plane deflection normalized by the analytical buckling strain e_{cr} (Fig. 13c) are shown as functions of the applied load P normalized by the analytical buckling load P_{cr}. The open circles in the figure represent test data and the curves represent analytical data determined from STAGS by a nonlinear analysis. The filled circle in Fig. 13a represents the bifurcation buckling load of the specimen determined from STAGS by a buckling calculation. These experimental and analytical results correlate well up to failure of the specimens.

The membrane strain distributions across the skin center bay at midlength from analysis and test are compared in Fig. 14 for four values of applied loading P normalized by the analytical buckling load P_{cr}. The y coordinate across the skin bay is measured from the left interior stiffener and normalized by the stiffener spacing b. The membrane strain e is normalized by the strain at buckling e_{cr}. The analytical results in Fig. 14 are represented by the open circles and the test results are represented by the curves. These results indicate that the analysis predicts the longitudinal membrane strain accurately in the skin up to failure.

A contour plot of the out-of-plane skin deflections generated from the STAGS postbuckling solution for the specimen U6 at an applied load of 445 kN is shown in Fig. 15a. Also shown in Fig. 15a are the shapes of the longitudinal and lateral components of this postbuckling solution at panel midwidth and midlength, respectively. A photograph of the moire-fringe pattern corresponding to the out-of-plane deflections observed during the testing of specimen U6 is shown in Fig. 15b at an applied load of 445 kN. These results indicate that the postbuckling out-of-plane skin deflections from both test and analysis have the same shape over the entire panel.

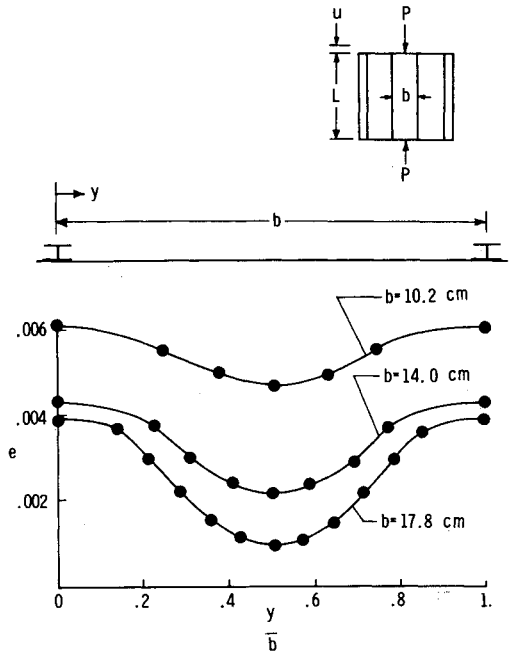

a) Panels with 24-ply skins.

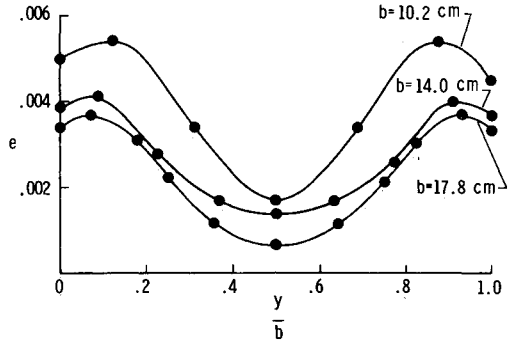

b) Panels with 16-ply skins.

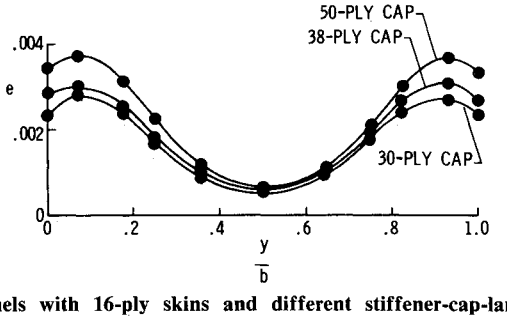

c) Panels with 16-ply skins and different stiffener-cap-laminate thicknesses.

Fig. 12 Longitudinal membrane strain distributions just before failure.

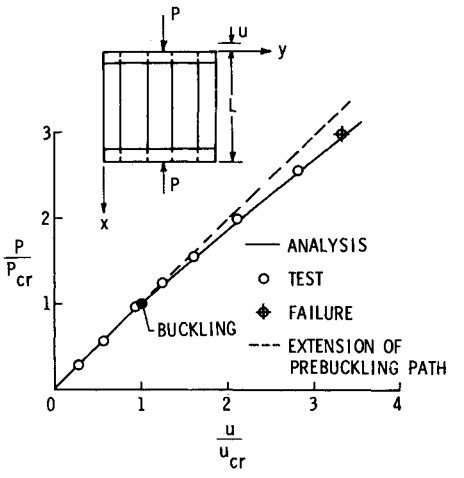

a) End-shortening results.

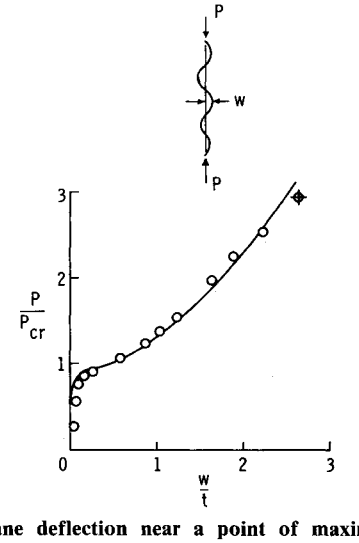

b) Out-of-plane deflection near a point of maximum buckling-mode amplitude.

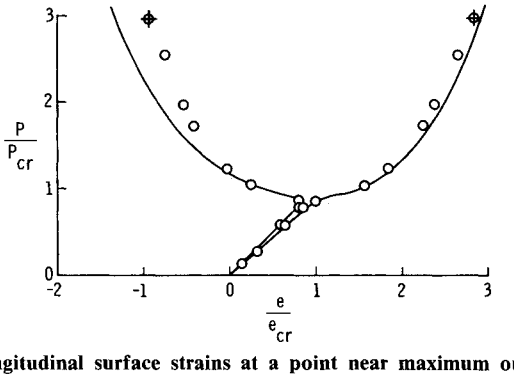

c) Longitudinal surface strains at a point near maximum out-of-plane deflection.

Fig. 13 Comparison of experimental and analytical postbuckling response results for specimen U6.

Impact-Damaged Specimens

The extent of damage caused by the 1.27-cm-diam aluminum projectiles impacting the specimens without any applied compressive load varied from barely visible to easily seen surface damage depending on the impact speed and location. An example of severe back-surface damage is shown in Fig. 16a for a typical 24-ply skin specimen impacted at a speed V of 100 m/s in the skin midway between two stiffeners. This visible damage extends across the skin along a 45 deg direction and is approximately 11 cm long and 2 cm wide. An ultrasonic C-scan of this impacted region indicates that the damage was distributed along the visible crack shown in Fig. 16a and approximately 3-4 cm wide.

Typical back-surface damage caused by a 103 m/s impact at the skin-stiffener interface region is shown in Fig. 16b for the same specimen. This visible damage in the interface region is a small rectangular area approximately 8 mm wide and extends across one side of the stiffener attachment flange. A C-scan of this impacted region indicates that the damage was localized to a region approximately 3-4 cm in diameter at the skin-stiffener interface region.

The effect of impact damage on the postbuckling response of the specimens tested in this investigation is shown in Fig.

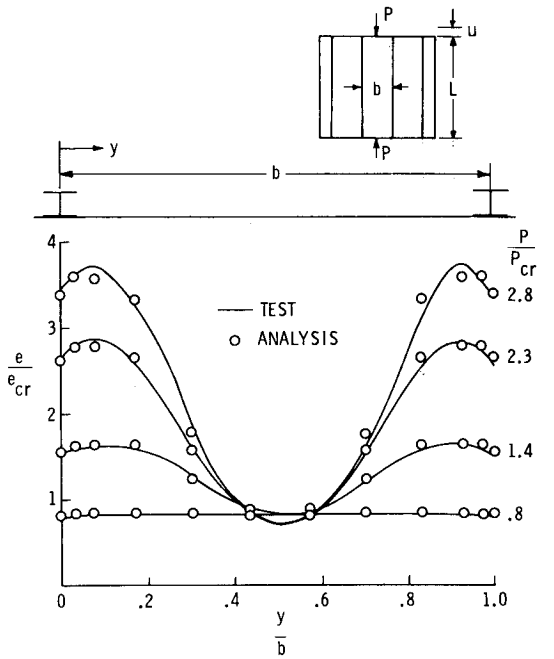

Fig. 14 Comparison of experimental and analytical membrane strain distributions across the center bay for specimen U6.

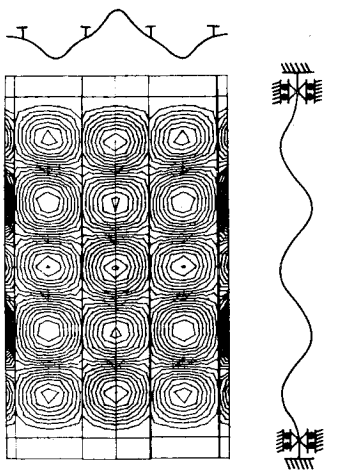

a) STAGS-generated contour plot of out-of-plane deflection pattern.

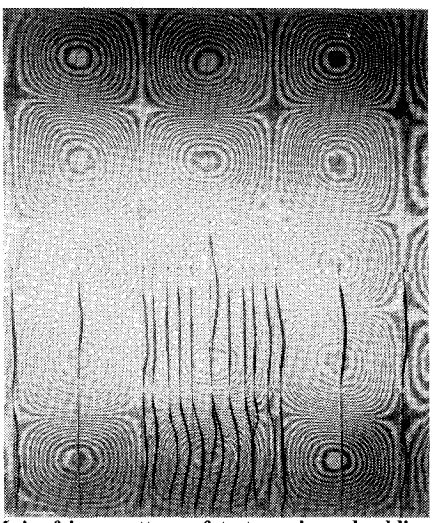

b) Moire-fringe pattern of test specimen buckling skin.

Fig. 15 Comparison of experimental and analytical out-of-plane deflection patterns for specimen U6 at an applied load of 445 kN.

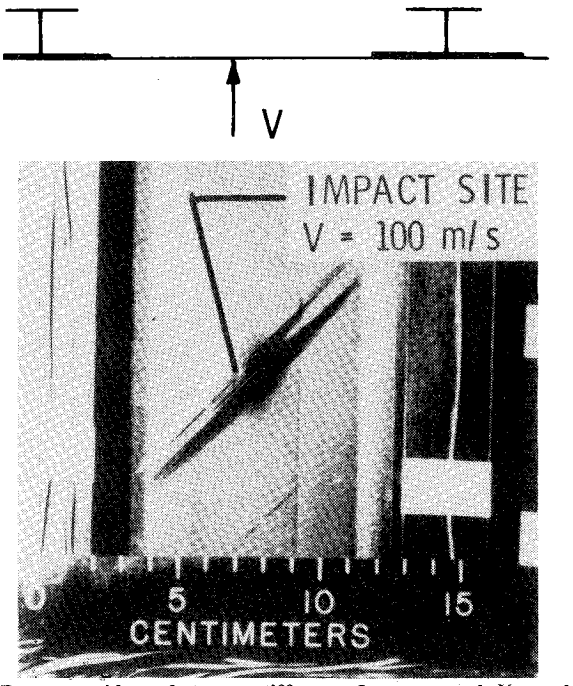

a) Damage midway between stiffeners. Impact speed V equal to 100 m/s.

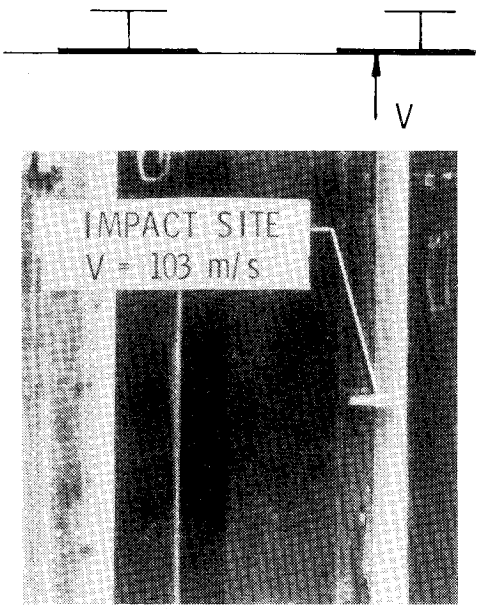

b) Damage at skin-stiffener interface. Impact speed V equal to 103 m/s.

Fig. 16 Impact damage in a specimen with a 24-ply skin and 10.2-cm stiffener spacing.

17. The measured end shortening u normalized by the specimen length L is shown in the figure as a function of the applied load P normalized by the prebuckling extensional stiffness EA. Initial buckling is indicated by the open circles on the figures and specimen failure is indicated by the filled circles. Data for three 24-ply skin specimens for each stiffener spacing are shown in Figs. 17a-c. For each stiffener spacing, one specimen was tested to failure with no impact damage ($V=0$), one specimen was tested after being impacted at two sites by projectiles with nominal speeds V of 70 m/s, and one specimen was tested after being impacted at two sites by projectiles with nominal speeds V of 100 m/s. Data for 16-ply skin specimens with 10.2- and 17.8-cm stiffener spacings are shown in Figs. 17d and 17e. For each stiffener spacing, one specimen was tested to failure with no im-

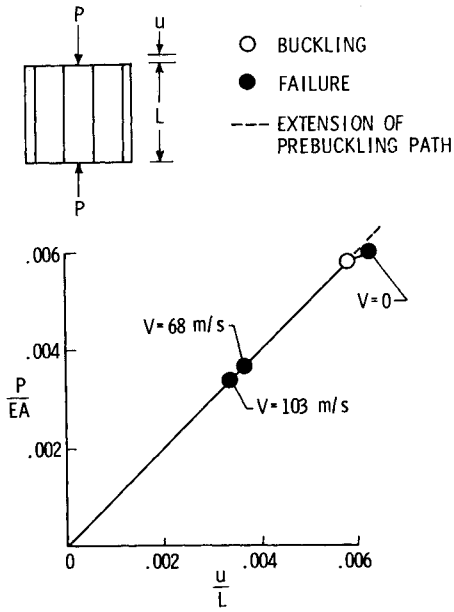

a) Panels with 24-ply skins and 10.2-cm stiffener spacing.

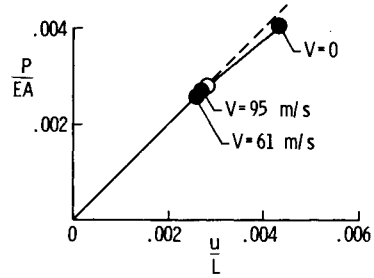

b) Panels with 24-ply skins and 14.0-cm stiffener spacing.

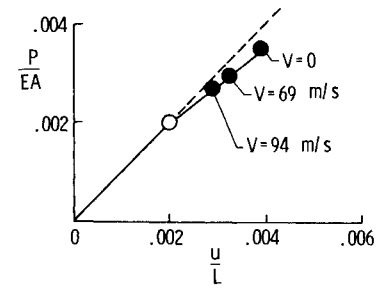

c) Panels with 24-ply skins and 17.8-cm stiffener spacing.

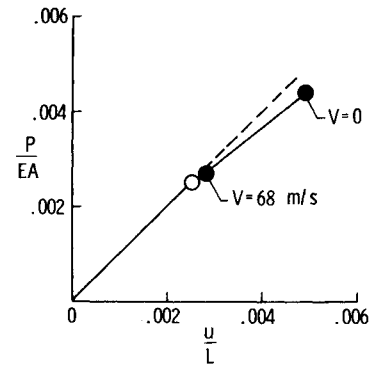

d) Panels with 16-ply skins and 10.2-cm stiffener spacing.

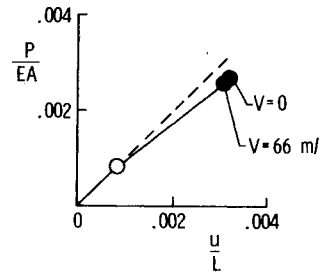

e) Panels with 16-ply skins and 17.8-cm stiffener spacing.

Fig. 17 Effect of low-speed impact damage on the compression strength of stiffened flat graphite-epoxy panels.

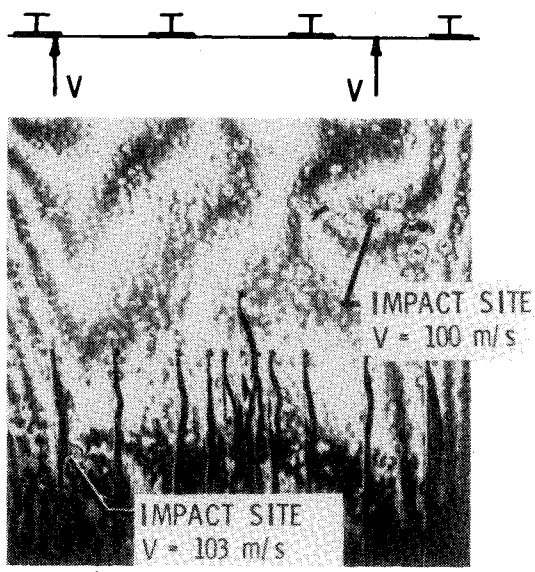

a) Moiré-fringe pattern of panel just before failure. Applied load equal to 489 kN.

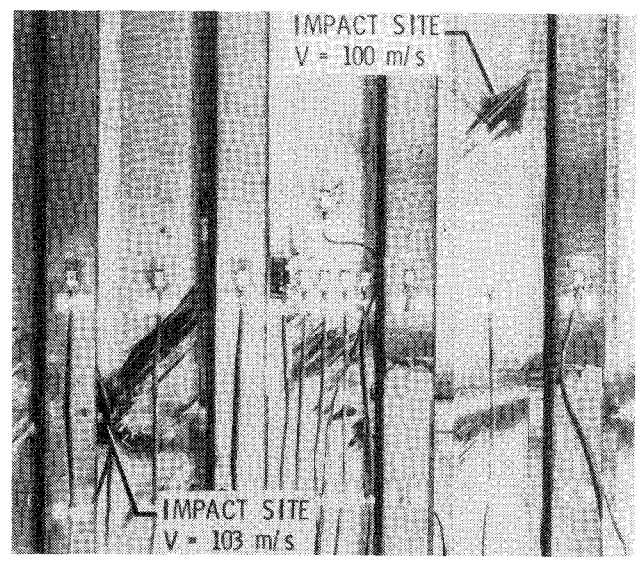

b) Rear view of panel after failure.

Fig. 18 Impact damaged panel with a 24-ply skin and 10.2-cm stiffener spacing.

pact damage ($V=0$), and the other specimen was tested after being impacted at the skin-stiffener interface region by a projectile with a nominal speed V of 70 m/s. Panel lengths, widths, stiffener spacings, failure loads and corresponding end shortening at failure, and projectile speeds are given in Table 4.

The results shown in Fig. 17 indicate that the compressive strength of the specimens can be degraded by low-speed impact damage. Impact-damaged specimens with 24-ply skins and 10.2-cm (Fig. 17a) or 14.0-cm (Fig. 17b) stiffener spacing failed before buckling. Damaged specimens having 24-ply skins with 17.8-cm stiffener spacing (Fig. 17c) and 16-ply skins with 10.2-cm stiffener spacing (Fig. 17d) failed after buckling. The postbuckling strength of the impact-damaged specimen having the 16-ply skin with 17.8-cm stiffener spacing (Fig. 17e) did not appear to be affected by the damage. These results indicate that specimens with the higher initial buckling strains appear to be affected more by low-speed impact damage than specimens with the lower initial buckling strains.

All impact-damaged specimens failed as a result of the damage inflicted at the skin-stiffener interface region. A front view of specimen D2 with two impact-damage sites is shown in Fig. 18a just before failure. The local impact-damaged regions are highlighted by moire-fringe patterns. The damage in the skin midway between stiffeners has propagated across the skin bay to the stiffeners, but the damage at the skin-stiffener interface region is still local to the stiff-

ener region. A rear view of this specimen after failure is shown in Fig. 18b. The failure of this typical specimen indicates that the impact damage at the skin-stiffener interface propagated to fail the specimen while the damage in the skin midway between stiffeners is still locally contained. It appears that damage in the skin-stiffener interface region can reduce the postbuckling strength of the specimens significantly by causing skin-stiffener separation to develop at lower loads than would occur otherwise.

Concluding Remarks

An experimental investigation was conducted to study the postbuckling behavior of selected flat stiffened graphite-epoxy panels loaded in compression. Sixteen panels with either 16- or 24-ply quasi-isotropic skins were tested in this investigation. Each panel had four equally spaced I-shaped stiffeners. Panels with three different stiffener spacings were tested. Some of the panels were subjected to low-speed impact damage to determine the effect of impact damage on the postbuckling response of the panels.

The buckling mode of all specimens tested was a stiffened-panel buckling mode in which both the stiffeners and skin deformed. Some of the undamaged specimens supported as much as three times their initial buckling loads before failing. Failure of all panels appeared to initiate in a skin-stiffener interface region. Apparently, the high membrane strains that exist at the stiffeners after skin buckling are sufficient to cause a local skin-stiffener separation that contributes to the overall panel failure.

Analytical results obtained from the STAGS nonlinear general shell analysis computer code correlate well with typical postbuckling test results up to failure. Since the analytical buckling mode had a considerable amount of deformation in the stiffener webs and attachment flanges, it was necessary to model these stiffener components with plate elements having the appropriate stiffnesses to obtain satisfactory correlation with the postbuckling test results.

The test results show that low-speed impact damage can reduce the postbuckling strength of a stiffened graphite-epoxy panel. The postbuckling strength of impact-damaged panels with high initial buckling strains was reduced more by impact damage than panels with lower initial buckling strains. Impact damage in a skin-stiffener interface region, where the postbuckling membrane strains are high, reduces the postbuckling compressive strength more than impact damage in the skin midway between stiffeners, where the membrane strains are relatively low.

References

[1]Turvey, G. J. and Wittrick, W. H., "The Large Deflection and Postbuckling Behaviour of Some Laminated Plates," *Aeronautical Quarterly*, Vol. 24, 1973, pp. 77-84.

[2]Harris, G. Z., "Buckling and Post-Buckling of Orthotropic Laminated Plates," AIAA Paper 75-813, 1975.

[3]Harris, G. Z., "The Buckling and Post-Buckling Behaviour of Composite Plates Under Biaxial Loading," *International Journal of Mechanical Sciences*, Vol. 17, 1975, pp. 187-202.

[4]Banks, W. M., "The Post Buckling Behaviour of Composite Panels," *Proceedings of the 1975 International Conference on Composite Materials*, ICCM, Vol. 2, 1976, pp. 272-293.

[5]Starnes, J. H. Jr. and Rouse, M., "Postbuckling and Failure Characteristics of Selected Flat Rectangular Graphite-Epoxy Plates Loaded in Compression," AIAA Paper 81-0543, 1981.

[6]Starnes, J. H. Jr., "Buckling and Postbuckling Research on Flat and Curved Composite Panels," *Selected NASA Research in Composite Materials and Structures*, NASA CP-2142, 1980, pp. 313-327.

[7]Dickson, J. N., Cole, R. T., and Wang, J. T. S., "Design of Stiffened Composite Panels in the Post-Buckling Range," *Fibrous Composites in Structural Design*, edited by E. M. Lenoe, D. W. Oplinger, and J. J. Burke, Plenum Press, New York, 1980, pp. 313-327.

[8]Dickson, J. N., Biggers, S. B., and Wang, J. T. S., "Preliminary Design Procedure for Composite Panels with Open-Section Stiffeners Loaded in the Post-Buckling Range," *Advances in Composite Materials*, edited by A. R. Bunsell et al., Pergamon Press Ltd., Oxford, England, 1980, pp. 812-825.

[9]Almroth, B. O. and Brogan, F. A., "The STAGS Computer Code," NASA CR-2950, 1980.

[10]Starnes, J. H. Jr., Rhodes, M. D., and Williams, J. G., "Effect of Impact Damage and Holes on the Compressive Strength of a Graphite/Epoxy Laminate," *Nondestructive Evaluation and Flaw Criticality for Composite Materials*, ASTM STP 696, edited by R. B. Pipes, American Society for Testing and Materials, Philadelphia, Pa., 1979, pp. 145-171.

[11]Anderson, M. S. and Stroud, W. J., "A General Panel Sizing Computer Code and Its Application to Composite Structural Panels," *AIAA Journal*, Vol. 17, Aug. 1979, pp. 892-897.

[12]Bushnell, D., "Evaluation of Various Analytical Models for Buckling and Vibrations of Stiffened Shells," *AIAA Journal*, Vol. 11, Sept. 1973, pp. 1283-1291.